CVD synthesis of polycrystalline magnetite thin films: structural, magnetic and magnetotransport properties

R Mantovan, A Lamperti, M Georgieva, G Tallarida, M Fanciulli

CVD synthesis of polycrystalline magnetite thin films: structural, magnetic, and magnetotransport properties

R Mantovan[1,3], A Lamperti[1], M Georgieva[1], G Tallarida[1] and M Fanciulli[1,2]

[1]Laboratorio Nazionale MDM CNR-INFM, Via C. Olivetti 2, 20041 Agrate Brianza (MI), Italy.

[2]Dipartimento di Scienza dei Materiali, Università di Milano Bicocca, Milano, Italy

E-mail: roberto.mantovan@mdm.infm.it

Abstract. Magnetite (Fe_3O_4) is predicted to be half metallic at room temperature and it shows the highest Curie temperature among oxides. The use of Fe_3O_4 thin films is therefore promising for spintronic devices such as magnetic tunnel junctions and magnetoresistive sensors. The structural, magnetic, and magnetotransport properties of magnetite are reported to be strongly dependent on the growth conditions. We have developed a very simple deposition chamber for growing thin magnetite films via a chemical vapor deposition process based on the $Fe_3(CO)_{12}$ carbonyl precursor. The structural, morphological and magnetic properties of the as deposited Fe_3O_4 films have been investigated by means of time of flight secondary ion mass spectrometry, grazing incidence X-ray diffraction, X-ray reflectivity, atomic force microscopy, conversion electron Mössbauer spectroscopy, and superconducting quantum interference device magnetometry. Magnetotransport measurements show magnetoresistance up to -2.4% at room temperature at the maximum applied field of 1.1 T. Resistivity measurements in the 100-300 K temperature range reveal that the magnetotransport properties of the Fe_3O_4 films are governed by inter-granular tunneling of the spin polarized electrons. The spin polarization is estimated to be around -16%. A possible route for increasing the spin-polarized performances of our magnetite films is proposed. We have also deposited Fe_3O_4/MgO/Co stacks by using a combined chemical vapor- and atomic layer- deposition process. The trilayer's hysteresis curve evidences the presence of two distinct switching fields making it promising for magnetite-based magnetic tunnel junction applications.

[3] Author to whom any correspondence should be addressed.

1. Introduction

Magnetite (Fe_3O_4) is a ferrimagnetic oxide with an extremely high Curie temperature, T_C ~ 860 K [1]. Fe_3O_4 crystallizes in the cubic inverse spinel structure where the Fe cations are located interstitially in a face centred cubic close packed arrangement of O ions, and distributed into two non equivalent A and B sublattices. The tetrahedral A sites are occupied by Fe^{3+} ions surrounded by four oxygen atoms, while the octahedral B sites host a mixture of Fe^{2+}/Fe^{3+} ions (1:1 ratio in the stoichiometric compound) surrounded by six oxygen atoms, $(Fe^{3+})_A(Fe^{3+}, Fe^{2+})_BO_4$ [1]. The Fe atoms in the A and B sites are coupled antiferromagnetically and the Fe^{2+} ions in the B site give the macroscopic (ferro)magnetic properties. The conductivity of Fe_3O_4 arises from the fast electron hopping between the Fe^{3+} and Fe^{2+} ions at the B sites. The Fe_3O_4 is predicted to be half metallic, i.e. with a full -100% spin polarization (P) arising from the negative electron spin polarization at the Fermi level [2, 3]. Because of its abovementioned intrinsic characteristics, magnetite is one of the most interesting materials for application as ferromagnetic (oxide) layer into spintronic devices [4]. Even though very high P values (-80 %) have been observed in epitaxial magnetite films [5], the possibility to obtain full spin polarization in this material is still disputed [4, 6]. The large number of recent publications on this topic underlines the high interest in this material [5-16], but the practical achievement of (the expected) high performances in functional spintronic devices like magnetic tunnel junctions (MTJ) incorporating Fe_3O_4 has not been reached yet [9-11, 13].

Thin Fe_3O_4 films are mainly produced by pulsed laser deposition [10-13], magnetron sputtering [7-9, 14, 15], and molecular beam epitaxy [16]. We propose a simple and cost-effective method for growing magnetite thin films based on a chemical vapour deposition (CVD) process [17]. Among the advantages of employing the chemical methods for the thin film synthesis, we mention the possibility of handling large area substrates, good conformality, and the relative low cost, factors making them very attracting in the view of possible industrial applications. We show by time of flight secondary ion mass spectrometry (ToF SIMS), grazing incidence X-ray diffraction (GIXRD), X-ray reflectivity (XRR), atomic force microscopy (AFM), conversion electron Mössbauer spectroscopy (CEMS), and superconducting quantum interference device (SQUID) magnetometry that good quality polycrystalline magnetite thin films can be deposited with our system. In the present paper we discuss the properties of 10-30 nm thick magnetite films. The samples exhibit magnetoresistance (MR) effect of few percent when the magnetic field is 1.1 T. The

magnetotransport properties of the deposited Fe_3O_4 layers are found to be governed by inter-granular tunnelling of spin polarized carriers. The electron spin polarization is estimated to be around -16%.

The first step toward the implementation of Fe_3O_4 into practical devices such as MTJs, is the growth of appropriate multilayers. We have synthesized Fe_3O_4/MgO/Co stacks by using either a chemical vapour (Fe_3O_4 and Co) or an atomic layer (MgO) deposition process [17]. The hysteresis curve of selected trilayers shows two distinct switching fields related to the Co and Fe_3O_4 coercive fields, evidencing that the proposed stack is promising for the synthesis of functional MTJs.

2. Experimental methods

2.1. CVD growth of Fe_3O_4 and synthesis of Fe_3O_4/MgO/Co trilayers.

We have synthesized magnetite thin films in the 10-30 nm thickness range by using a CVD setup based on horizontal furnace equipped with a 4 cm diameter quartz tube [17]. We have used the metalorganic triiron dodecarbonyl $Fe_3(CO)_{12}$ precursor, which is solid (but extremely volatile) at room temperature (RT) and at ambient pressure. A bubbler system containing the precursor is sealed to the end of the quartz tube. At the opposite side, the vacuum is granted by a pumping system able to lower the pressure down to $1x10^{-4}$ mbar. The $Fe_3(CO)_{12}$ precursor can be easily decomposed through thermal cycles, due to its low melting point (165 °C) and the low activation energy of the decomposition process, i.e. the separation of the metal atom with the formation of CO and CO_2 gases. The complicate interplay among the precursor's temperature and pressure, and the substrate temperature, plays a fundamental role in determining the final film composition. Our films are deposited on Si/SiO_2 (550 nm) substrates over a ~2 x 2 cm^2 area, and are accommodated vertically in the quartz tube. We have not observed differences in the film surface roughness (from XRR) as a function of the substrate temperature in the 200-400 °C range. Since the highest grow rate is observed at 400 °C, this has been identified as the optimal deposition temperature. We have used Ar as carrier gas and the precursor temperature is kept at 50 °C during deposition, thus favouring and accelerating the precursor's evaporation process. Table 1 summarizes the growth conditions of the selected films, together with their thickness, roughness, and electronic density as calculated by XRR; surface roughness measured by AFM is also reported.

Table 1. Description of the set of Fe_3O_4 samples that are discussed in the paper. The films are deposited by using the $Fe_3(CO)_{12}$ precursor kept at 50 °C, on Si/SiO_2 substrates heated at 400 °C. Film thickness, roughness, and electronic density are derived from XRR spectra; surface roughness measured by AFM is also reported.

Samples	Deposition pressure (10^{-3} mbar)	Deposition time (min)[a]	XRR, thickness/ roughness (nm)	XRR, electronic density ($e^-/Å^3$)	AFM surface roughness (nm)
Fe20	5.8÷7.5	10	28.9(1) / 3.3(1)	1.48(5)	3.2(3)
Fe28	5.3÷6.9	3	16.1(1) / 2.2(1)	1.47(5)	1.1(1)
Fe29	5.4÷7.7	1	12.8(1) / 2.3(1)	1.41(5)	0.9(1)

[a]the first (unstable) 1÷2 minutes deposition are not considered.

Prior to the deposition, the chamber is evacuated at $1x10^{-4}$ mbar for several minutes. When the precursor is introduced in the chamber, pressure experiences some instability; at this stage (1-2 min) film deposition starts, although growth parameters are not easily controlled, and after the pressure reaches its equilibrium value of $5÷8 \times 10^{-3}$ mbar, which remains constant throughout the film growth. Figure 1 reports the grow rate of the Fe_3O_4 films listed in table 1. The repeatability of the process for obtaining Fe_3O_4 has been assessed by a large number of samples produced in similar experimental conditions.

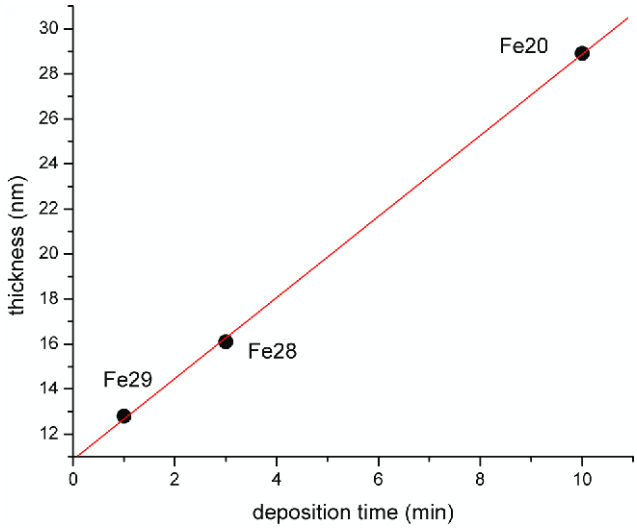

Figure 1. Grow rate of the Fe_3O_4 films listed in table 1. The red line shows a linear fit of the samples thickness depending on different deposition times.

By using the same $Fe_3(CO)_{12}$ precursor, but working at $\sim10^{-5}$ mbar (at 200 °C) in a vertical-geometry CVD apparatus, Boyd *et al.* were able to deposit pure Fe films [18], suggesting that the deposition pressure plays a key-role in governing the composition of the films. At our experimental conditions, the formation of

Fe_3O_4 compound instead of pure α-Fe has two possible explanations. (a) The oxygen comes from the dissociation of CO groups at the Fe surface during the growth and/or (b) the Fe oxidation is a consequence of the relatively low vacuum that is used during the deposition (10^{-2}÷10^{-3} mbar). It has been shown that during the Fe carbonyls decomposition, some CO molecules could be chemisorbed and dissociated at the surface of Fe particles leading to the formation of Fe oxides and Fe carbides [19-21]. However, the extremely low C content observed from ToF SIMS profiles (Section 3.1) indicates that Fe carbides, if present, are less than 1÷2 at%, and this is confirmed by the absence of such phases in the GIXRD and CEMS spectra (Sections 3.1 and 3.3). Our experimental results support that the formation of Fe oxide origins mainly from the deposition atmosphere at the particular growth conditions.

Further, we deposited Fe_3O_4/MgO/Co stacks by using a hybrid chemical vapour- and atomic layer-deposition (ALD) process. In particular, MgO thin films have been deposited on top of the magnetite films at 225 °C by using a conventional F-120 ASM-Microchemistry ALD reactor [17]. Finally, Co films have been deposited (at 190 °C) on top of MgO by employing the same CVD system used for Fe_3O_4 growth [17].

2.2. Characterization techniques

Different and complementary experimental techniques are employed for studying the structural, morphological, chemical, magnetic, and magnetotransport properties of the deposited magnetite films. Our attention is particularly directed to the understanding of the most critical issues in view of the inclusion of magnetite thin films into spintronic devices, i.e. low roughness, uniform composition, film granularity, and high magnetoresistance of the layers.

Film composition has been studied with ToF SIMS depth profiling using an IONTOF IV instrument with Ga^+ ions at 25 keV for analysis and Cs^+ ions at 1 keV for sputtering. All data have been acquired in interlaced mode, negative polarity, rastering Cs^+ and Ga^+ ion beams over a 200 x 200 and 50 x 50 μm^2 area, respectively.

GIXRD, at incidence angle ω=1°, and XRR have been used to investigate the crystalline structure and the films thickness and roughness. These measurements have been acquired using an upgraded XRD3000 (Italstructure) diffractometer with monochromated X-ray Cu Kα radiation (wavelength 0.154 nm) and a

scintillator type point detector in XRR geometry or a position sensitive detector (Inel CPS120) in GIXRD.

AFM measurements were acquired in non-contact mode, using a commercial system. Ultrasharp silicon probes (nominal tip radius ~10 nm) were used and several scans were taken on both 1x1μm^2 and 2.3x2.3 μm^2 areas for each samples. From the data acquired on 2.3x2.3 μm^2 areas, the surface root mean square (rms) roughness was extracted, which accounts for the height fluctuations of surface features [22]. To provide a measure of the lateral fluctuations of such features, the correlation length ξ, defined as the characteristic length at which the autocorrelation function of the image data decays to 1/e, is also calculated for each sample [22].

We have used ^{57}Fe-CEMS for studying the atomic-scale structural, chemical, and magnetic properties of the Fe_3O_4 films. Our films contain only the natural 2.2% abundance of the (Mössbauer active) ^{57}Fe isotope. CEMS has been carried out by using a ^{57}Co source (activity ~7 mCi) that is moved by a standard constant acceleration drive. The samples are incorporated as one of the electrodes in a parallel plate avalanche counter filled with He-CH_4 gas mixture at a pressure of 180 mbar. The operating voltage is ~700÷800 V [23].

The magnetic properties of the deposited films have been investigated by using the quantum design magnetic property measurements system (MPMS) magnetometer, employing SQUID as detector of the magnetic moment. All hysteresis loops have been measured at RT and in a broad range of magnetic fields up to 5 T applied in the sample plane.

Resistivity measurements have been performed using a four points probe following the Van der Pauw method. MR measurements have been performed with both two and four terminal configurations (the two configurations giving same results) in applied magnetic fields up to 1.1 T at RT and up to 0.8 T at 100 K. The field was applied in the film plane for low temperature measurements, and both parallel and perpendicular to the sample plane at RT.

3. Results and discussion

3.1. Structural, morphological, and chemical characterization of Fe_3O_4 films and Fe_3O_4/MgO/Co trilayers.

Figure 2 shows the GIXRD and XRR measurements for the samples described in table 1.

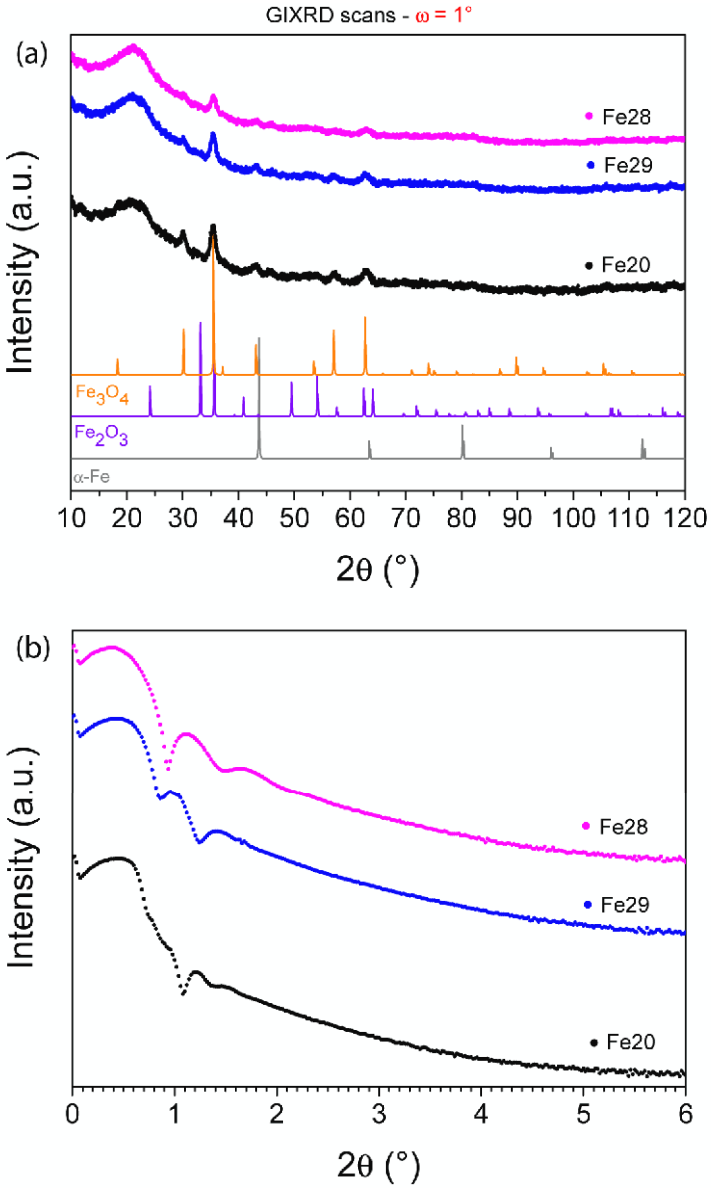

Figure 2. (a) GIXRD (incidence angle ω=1°) and (b) XRR experimental scans for the magnetite films reported in table 1. Reference powder diffraction patterns for Fe_3O_4, Fe_2O_3 and α-Fe are also shown.

GIXRD identifies the phase of the films to be polycrystalline Fe_3O_4, as shown in figure 2 (a), where bulk Fe_3O_4, α-Fe_2O_3 and α-Fe reference diffraction patterns are also reported [24-26]. The electron densities in bulk α-Fe, α-Fe_2O_3 and Fe_3O_4 are 2.11, 1.39 and 1.45 $e^{-}Å^{-3}$, respectively. From XRR analysis shown in figure 2(b), the extracted electron density values (table 1) for our samples are very close to the value expected for bulk Fe_3O_4, confirming that our films mainly consist of magnetite. The roughness values from XRR are in the range 2-4 nm. Grain size plays a major role in shaping the macroscopic magnetic properties of the magnetite thin films, as it will be substantiated in section 3.2. The Fe_3O_4 grain size was estimated from

Scherrer analysis on the $(2\bar{1}0)$ peak at 2θ=35.4° to be in the range 8.97(1)-9.34(1) nm, depending on film thickness. It should be noted that the grain size obtained using Scherrer equation must be seen as an inferior limit of the grain size, because the method does not take into account the contribution to line-broadening associated i.e. with the presence of stress; in our thin films the presence of stress and/or stress gradient cannot be excluded mainly due to the (non equilibrium) thermodynamic deposition process.

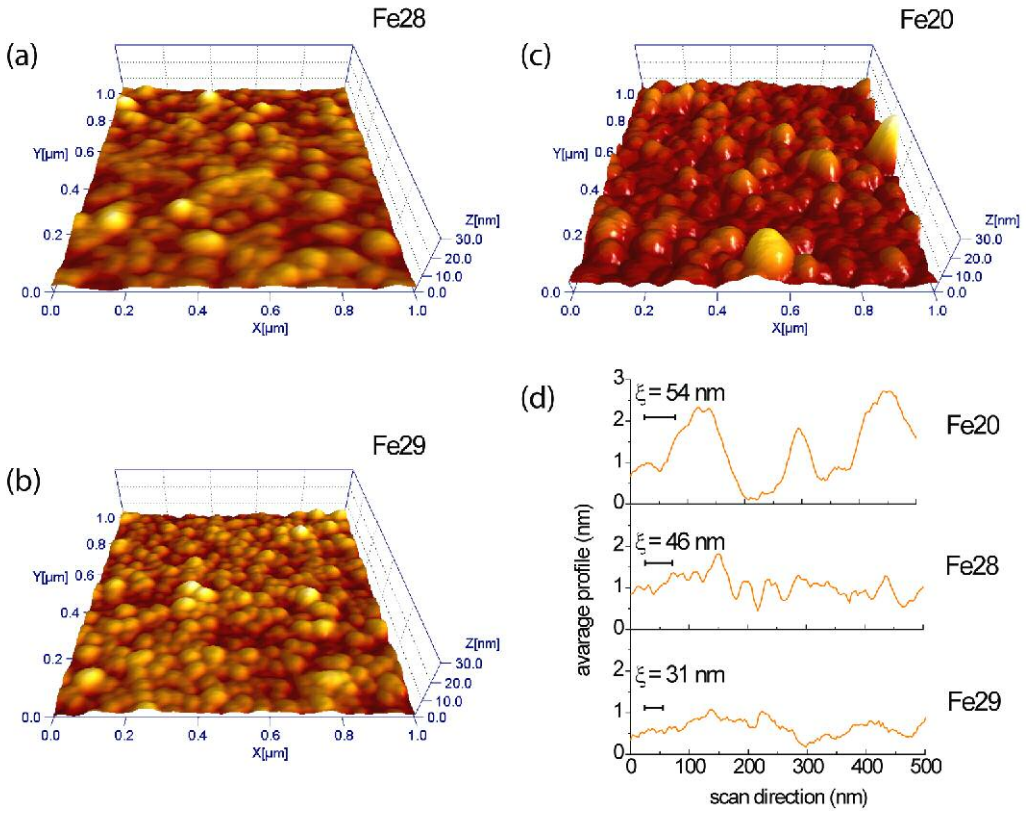

Figure 3. AFM surface morphology of samples (a) Fe28, (b) Fe29, and (c) Fe20; scan area is 1x1 μm^2; (d) average line profile along y direction for each image; the correlation length ξ derived from the autocorrelation function of 2.3x2.3 μm^2 images is also reported for each sample.

AFM topographic images in figure 3 evidence the granular nature of the films, all consisted of highly packed grains. The grain size is seen to scale with the film thickness. Differences among samples are further evidenced by comparing the average line profile, figure 3(d), where the increase in vertical and lateral fluctuations of surface features, moving from sample Fe29 to sample Fe20, is clear. Indeed, surface rms roughness (table 1) increases with samples thickness, as already deduced by XRR. Discrepancies respect to

XRR in the roughness values for samples Fe28 and Fe29 can be ascribed to the size of the AFM probe tip, which might smooth smaller features. On the other hand, XRR fitting models do not distinguish between topography and density fluctuations, which are both considered as roughness; therefore a certain overestimation of XRR roughness data with respect to AFM values is not surprising.

Since films consist of well packed grains, it is not possible to determine the grain size by AFM directly. Thus, we use the correlation length ξ to account for the width of surface features, finding ξ =31, 46, and 54 nm for Fe29, Fe28, and Fe20 respectively. AFM results strongly suggest that the size of the grains increases with the thickness, in agreement with GIXRD findings.

The purity of the magnetite films is investigated using ToF-SIMS depth profiling. The analysis evidences nice flat profiles for the FeO signal, an indication of a good degree of chemical composition and in-depth uniformity of the film, as shown in figure 4 for sample Fe28. Further, the presence of contaminations is very low. A typical source of contamination for the films deposited by CVD is carbon, as it is a major constituent of the precursor and it may happen that it is not completely evacuated during the growth process and incorporated in the growing film. As seen in figure 4, the C signal has an intensity equivalent to a concentration of less than 1-2 at. %; in fact, a large concentration of C in the films, would lead to a signal saturation in the depth profile, due to the extreme sensitivity of ToF SIMS.

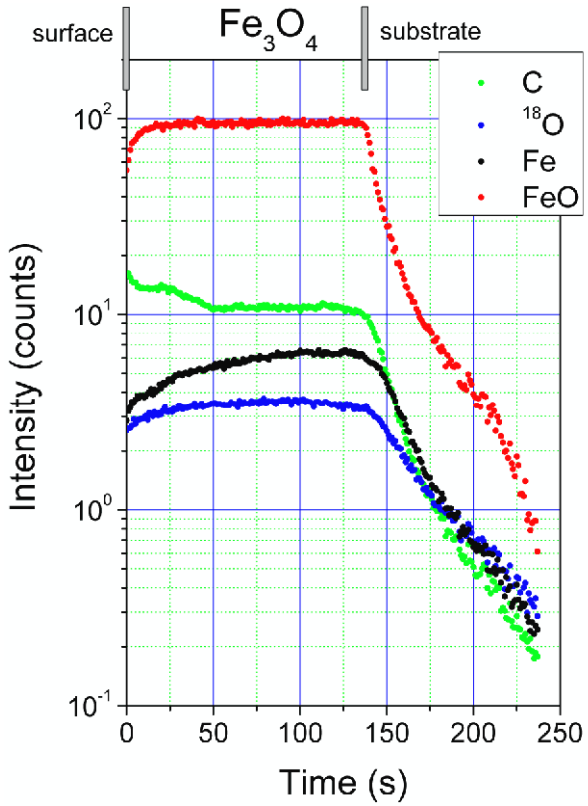

Figure 4. ToF SIMS depth profile of the Fe28 sample.

XRR measurements have been performed on a representative Fe_3O_4/MgO/Co stack. The XRR fitting analysis determined a model structure consisting of Co(28.0 nm)/MgO(6.5 nm)/Fe_3O_4(16.1 nm) trilayer. The surface roughness is 3.4 nm and the Co/MgO and MgO/Fe_3O_4 interfaces roughness are 2.4 and 3.9 nm respectively. ToF SIMS profiles of the trilayer clearly show (figure 5) the various layers composing the stack from the surface (from left to the right in figure): CoO, Co, MgO, Fe_3O_4 and the SiO_2/Si substrate. From the depth profile in figure 5, it is possible to discriminate a sub-surface region where the Co film appears oxidized, detected as an intense and flat CoO profile, followed by a region of pure Co film, as denoted by the sharp drop of the CoO intensity while, in the same region, the Co decrease is limited. Despite the surface or interface roughness, the character and uniformity of each layer is preserved during the deposition process, as evidenced by the profile flattening in each constituent layer. As clearly shown in figure 5, no major intermixing is found at the interfaces, i.e. the layered structure of the stack is preserved. The less defined interface is MgO/Fe_3O_4 while the Co/MgO interface appears sharp in agreement with the interface roughness values from XRR. In fact, figure 5 evidences almost no MgO interdiffusion takes place at the Co/MgO interface. The tails of the CoO and Co intensities, which are seen to partially propagate inside the MgO layer, quickly decay following a linear trend and are due to the knock-on effect related with the sputtering process. Contaminations (not shown) are kept at low-level concentration, as in the Fe_3O_4 layer.

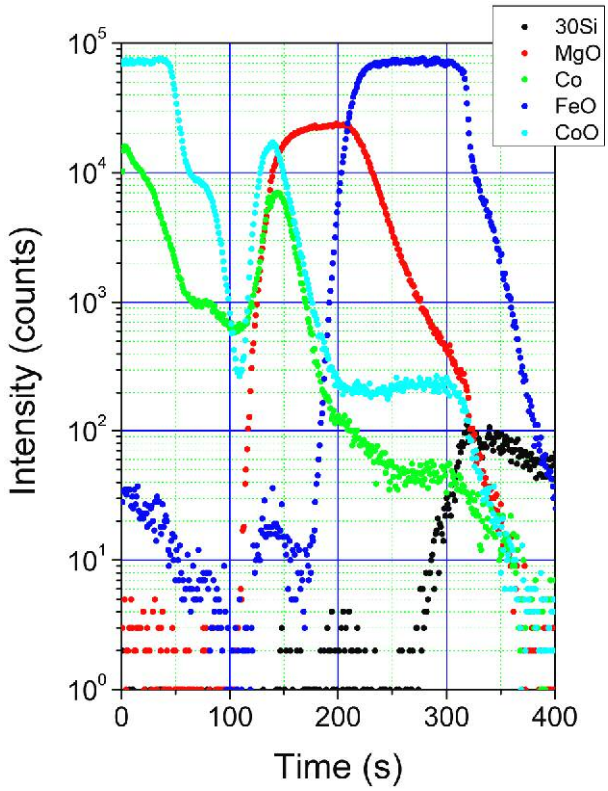

Figure 5. ToF SIMS depth profile of a Co/MgO/Fe_3O_4 stack grown on SiO_2/Si substrate.

3.2 Magnetic properties of the Fe_3O_4 films.

SQUID measurements have been performed at RT on all samples. Figure 6 shows a representative hysteresis loop, obtained from sample Fe20.

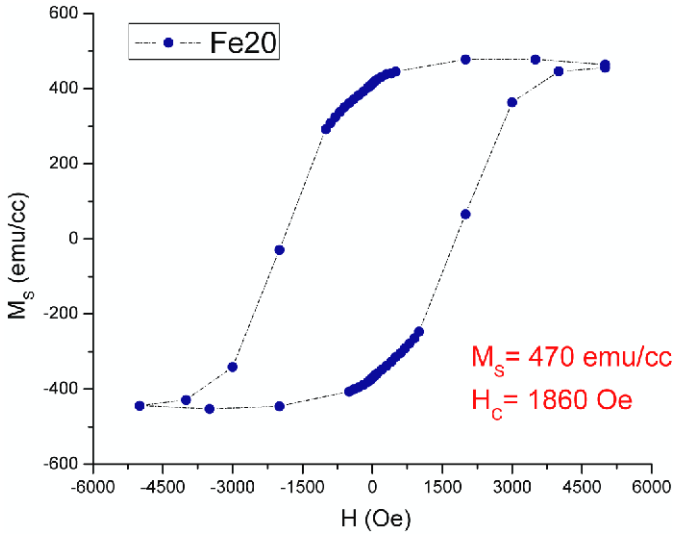

Figure 6. Hysteresis curve of sample Fe20, as measured by SQUID at RT.

Table 2 summarizes the SQUID results, i.e. the saturation magnetization (M_S) and the coercive field (H_C), for the samples listed in table 1.

Table 2. SQUID results for the samples Fe28, Fe29, and Fe20.

Sample	M_S (emu/cc)	H_C (Oe)
Fe29	600	180
Fe28	470	750
Fe20	470	1860

Even though the structural characteristics of the samples are very similar (XRD results), it is clear from table 2 that the macroscopic magnetic behaviour is different. Samples Fe28 and Fe20 show the typical M_S for the bulk Fe_3O_4 (~470 emu/cc). Sample Fe29 shows M_S ~600 emu/cc, higher than in bulk magnetite. We attribute this higher magnetization to the presence of small amount of α-Fe, probably in the amorphous phase. The values of the coercivity H_C are quite different among the samples. Since the H_C is an extrinsic parameter, it strongly depends on the growth conditions, the films morphology, and the grain size. Indeed, a large scattering exists in the H_C data reported in the literature for the magnetite films [1, 9, 14, 15]. We attribute the difference in the H_C values in our films to the coexistence of two effects: (i) the different grain size (XRD and AFM results, Section 3.1), and (ii) the marked difference in the vacancy concentration in the different samples (CEMS results, Section 3.3). In particular, the correlation lengths evaluated by AFM scale with H_C in a way that is consistent with the expected behaviour for single domain magnetite particles in the stable regime [1]. In general, for an inclusion of ferromagnetic films into spintronic devices such as MTJs, it is important to control the surface roughness and the coercivity of the ferromagnetic films, the former being responsible for spin-flip processes at the interface and the latter controlling the independent switching of the ferromagnetic electrodes. We observe limited surface roughness in Fe29 and Fe28 (table 1) and the coercivity of the Fe_3O_4 layers is seen to depend on the film thickness (table 2). In section 3.5 we show that independent switching of ferromagnetic layers is achieved for a Fe_3O_4/MgO/Co stack where 16 nm thick Fe_3O_4 and 28 nm thick Co films are employed.

3.3. Atomic scale characterization and magnetotransport properties of Fe_3O_4 films.

All samples were measured by CEMS for an atomic-scale structural, chemical, and magnetic

characterization. Figure 7(a) shows the CEM-spectrum of sample Fe20.

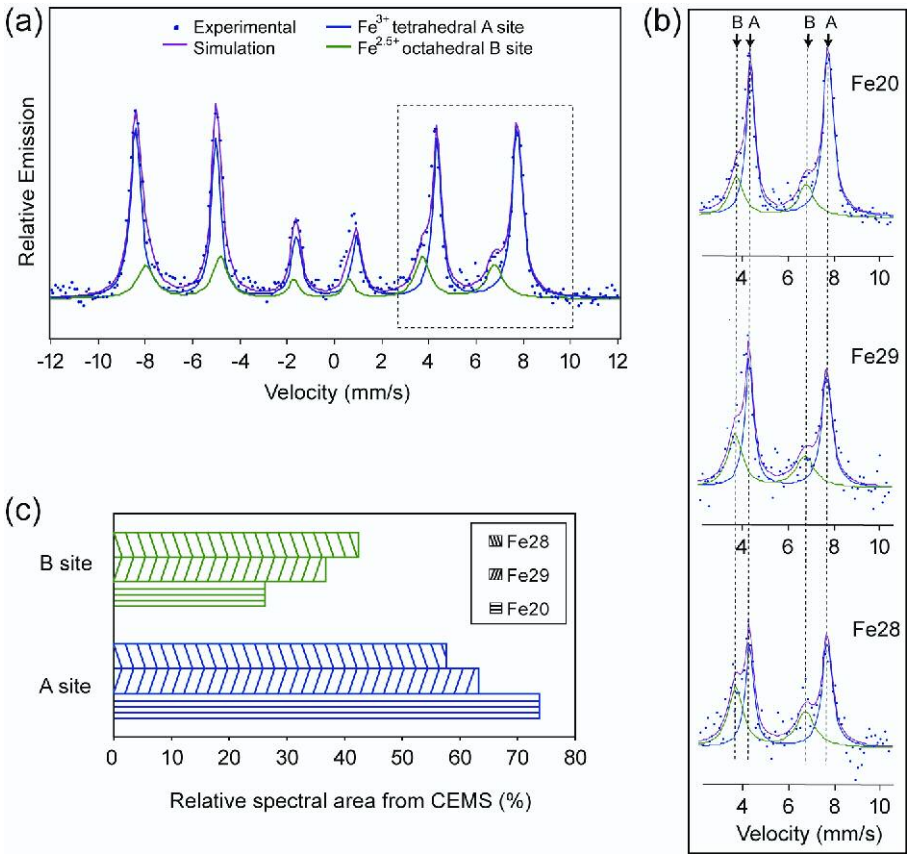

Figure 7 (a) CEM-spectrum of the Fe20 sample, showing the presence of the two characteristic magnetically-split sextets of magnetite A and B; (b) CEM-spectra region boxed in (a) for samples Fe20, Fe29, Fe28; (c) relative contribution to the Mössbauer total spectral intensity given by the Fe ions at the A and B sites of the magnetite crystal structure.

The Mössbauer spectrum of sample Fe20 can be interpreted by the superposition of two distinct magnetically-split sextets, indicated with A and B, which are typically observed in magnetite [27, 28]. These two sextets correspond to the tetrahedral A site and the octahedral B sites of the Fe_3O_4 crystal structure. The hyperfine parameters of the sextets are very similar to those reported for bulk magnetite [28]. The Mössbauer lines of the B sextet show a marked broadening, suggesting the possible presence of vacancies around the iron atoms [29]. Similar evidences have been previously attributed to the very fast hopping of the sixth 3d electron between the Fe^{2+} and Fe^{3+} ions residing at the octahedral B sites of Fe_3O_4 [28, 30].

CEMS is a powerful technique for evaluating the stoichiometry degree of magnetite by considering the area ratio (A/B) of the Mössbauer sextets in the CEM-spectrum [27]. Even though the CEM-spectra statistics

is not very high (due to low film thickness containing only the natural 2.2% ^{57}Fe abundance), there are marked differences in the A/B intensity ratio that are observed in the different samples, figure 7(b). The best fit of the experimental data is obtained for sample Fe20, figure 7(a), and the same fitting model (isomer shift, quadrupole splitting and hyperfine magnetic field) is then used for analyzing the Fe28 and Fe29 Mössbauer spectra. The relative line intensity of a magnetically-split sextet is 3:*x*:1:1:*x*:3, where $x=4\sin^2\theta/(1+\cos^2\theta)$ and θ is the angle between the γ-rays and the hyperfine field. In Fe20, the average *x* for the A and B sextets is 2.8(3), indicating that there is a slight out of plane component of the magnetization. Samples Fe28 and Fe29 show x =3.3(5) and x =3.4(5) respectively, indicating that in Fe28 and Fe29 the shape anisotropy plays a stronger role than in Fe20, with the magnetization being more aligned in the films plane. The relative sextets-intensity variation in the Mössbauer spectra of the different samples is reported in figure 7(c). The cation distribution at the two non-equivalent A and B Fe sites (n_A, n_B) can be determined by multiplying A/B by the Mössbauer recoilless fraction ratio f_B/f_A. Early measurements of the Debye-Waller factors for Fe at the A and B sites gave f_B/f_A=0.94 at RT [31], but later on it has been shown that the vibrational properties at those two sites are practically equivalent [32]. We consider f_B/f_A =1. With this assumption, the relative intensity ratio in the Mössbauer spectra A/B equal the A and B site population ratio $\beta\equiv n_A/n_B$. For stoichiometric Fe_3O_4 we expect $\beta\equiv0.5$, while the β parameter largely increases in the presence of vacancies ( ) at the B sites [27]. The vacancy concentration δ is an indication of the stoichiometry degree of the magnetite films. The non-stoichiometric $Fe_{3-\delta}O_4$ formula can be expressed as $(Fe^{3+})_A(Fe^{3+}_{1+2\delta}\ Fe^{2+}_{1-3\delta}\ \ _{\delta})_B O^{2-}_4$ by considering charge compensation. If every vacancy traps a Fe^{3+} ion and considering the electron hopping at the B site we obtain: $(Fe^{3+})_A(Fe^{2.5+}_{2-6\delta})_B\ (Fe^{3+}_{5\delta}\ \ _{\delta})_B O^{2-}_4$ [27]. The relationship between the cation distribution given by β and the vacancy parameter δ is expressed with Eq. (1).

$$\beta = \frac{1+5\delta}{2-6\delta} \qquad (1)$$

Table 3 shows the evaluation of the non-stoichiometry degree of our films as determined by CEMS, together with the vacancy parameter δ, as estimated by following an approach similar to that illustrated in [27]. The actual films composition is indicated as well.

Table 3. The cation distribution at the A and B sites (β) as determined by CEMS, the vacancy parameter (δ) as estimated with Eq. (1), and the chemical formula that considers the vacancy abundance.

Sample	β	δ	Film composition
Fe20	2.83	0.21(2)	$(Fe^{3+})_A(Fe^{2.5+}_{0.74})_B\,(Fe^{3+}_{1.05\quad 0.21})_B O^{2-}_4$
Fe28	1.36	0.13(2)	$(Fe^{3+})_A(Fe^{2.5+}_{1.22})_B(Fe^{3+}_{0.65\quad 0.13})_B O^{2-}_4$
Fe29	1.72	0.16(2)	$(Fe^{3+})_A(Fe^{2.5+}_{1.04})_B(Fe^{3+}_{0.8\quad 0.16})_B O^{2-}_4$
Stoichiometric Fe_3O_4	0.5	0.0	$(Fe^{3+})_A(Fe^{2.5+}_{2})_B\,O^{2-}_4$

Considering the δ values in our samples, we observe that they are highly non-stoichiometric, especially Fe20. This implies that a significant fraction of the Fe^{3+} ions residing at the B sites does not take part to the $Fe^{3+} \leftrightarrow Fe^{2+}$ electron hopping process, therefore lowering the sample's conductivity. This is clearly reflected in the CEMS spectra, where part of the Fe^{3+} ions at the B site contributes to the intensity of the A site-sextet (figure 7). The full oxidation of magnetite films (δ=1/3) would form the (metastable) maghemite phase γ-Fe_2O_3, which is a ferrimagnetic insulator due to the absence of Fe^{2+}, thus preventing the $Fe^{3+} \leftrightarrow Fe^{2+}$ hopping process. The Mössbauer spectra of pure γ-Fe_2O_3 show the presence of a single magnetically-split Fe^{3+} sextet. The presence of vacancies can strongly influence the extrinsic magnetic properties of our magnetite layers, like their switching field H_C. CEMS results suggest that the large difference in the H_C values observed in SQUID measurements (table 2), could be partly due to the different stoichiometry of the grains in addition to the different grain sizes.

Rogalski *et al.* [33] reported about the growth of non-stoichiometric magnetite films by oxidizing (at 400 °C and 10^{-1} mbar) FeS films deposited by CVD. Voogt *et al*. observed that non-stoichiometric magnetite can be obtained when the pressure of a NO_2 oxidizing gas is ≥ 1 x 10^{-3} mbar [27]. Even though our deposition method and procedure differ from those reported in [27, 33], the relatively high vacancy concentration in our films could mainly relate with the (relatively high) deposition pressure (Section 2.1).

The resistivities (at RT) of our samples are in the range 0.45 ÷ 4.55 Ωcm, being 2÷3 orders of magnitude higher than the value measured for the bulk Fe_3O_4 (4 x 10^{-3} Ωcm). Such a high resistivity for granular

magnetite has been previously reported, being attributed to the scattering and/or tunnelling of spin polarized carriers at the interfaces between adjacent grains [15]. The variation of the resistivity for sample Fe28 has been measured in the 100-300 K temperature range, as shown in figure 8.

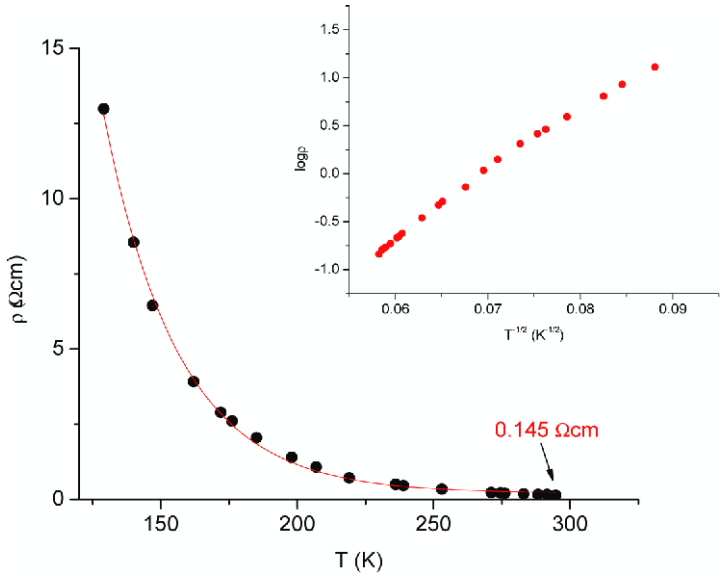

Figure 8. The resistivity of sample Fe28 in the 100-300 K temperature range shows an exponential behaviour leading to an almost linear dependence of logρ vs $T^{-1/2}$ (inset).

Figure 8 shows a clear, gradual, metal-insulator transition as the temperature decreases. The film does not show the sharp change of resistivity typically seen in bulk magnetite at the Vervey transition temperature (120 K). The broadening (sometimes disappearance) of the Verwey transition has been previously observed in polycrystalline magnetite thin films produced by magnetron sputtering [7, 15, 34-37]. The reason for the broadening/disappearance of the Verwey transition is often attributed to cation deficiency (i.e. vacancy abundance) [34, 35] and/or to the high resistivity at the grains boundaries [7, 36, 37]. The resistivity of polycrystalline Fe_3O_4 films is usually higher than the value measured in epitaxial films and single crystals, and the reason is the typical inter-granular tunnelling mechanism that drives the conduction process in polycrystalline magnetite [7, 15, 36, 37].

By considering our Mössbauer results, we also attribute the absence of the Vervey transition in Fe28 to the presence of a large amount of vacancies (table 3). The inset of figure 8 shows an almost linear dependence of logρ vs $T^{-1/2}$, demonstrating that the transport properties in our films are dominated by the inter-grain tunnelling of electrons, a mechanism determining the magnetotransport properties of (polycrystalline) magnetite thin films [15, 38, 39].

Figure 9(a) shows the MR of sample Fe28, as measured at 300 K with an applied magnetic field up to 1.1 T applied both parallel and perpendicular to the film plane. MR is defined as $MR=[R(H)-R_{max}]/R_{max}$, being R(H) and R_{max} the resistance in an applied field H and the maximum resistance, respectively.

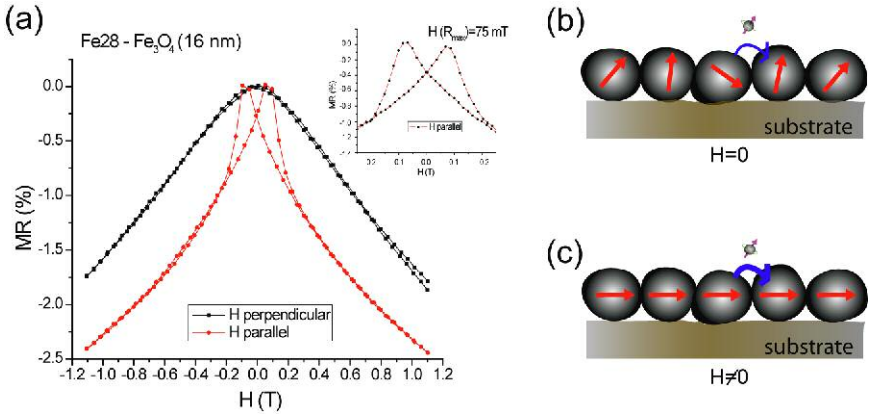

Figure 9. (a) MR measurements at RT of sample Fe28 for an applied field up to 1.1 T applied both parallel and perpendicular to the film plane; (b) without an applied magnetic filed, the magnetizations of the grains are almost randomly oriented and the tunnelling process is not favoured (higher film resistance) and this picture corresponds to the peaks in the MR curve; (c) by applying a magnetic filed the magnetizations of the grains are aligned, thus providing a more favourable tunnelling condition for the spin polarized electrons. In (b) and (c) the red arrows represent the magnetization direction in the grains and the blue arrows indicate the electron tunnelling process.

The inset of figure 9(a) shows a reduced field scan of MR that locates the maximum resistance at 75 mT, in agreement with the coercivity field measured by SQUID (table 2). At the maximum field, the MR of Fe28, Fe29, and Fe20 films are around -2.4 %, -2.0%, and -1.6% respectively. The MR of Fe28 has been also measured at 100 K, where it reaches the maximum value of -3.5 % at the maximum applied field (0.8 T). The MR characteristics observed in the magnetite films produced by CVD are compatible with those observed in polycrystalline Fe_3O_4 films produced by sputtering at similar applied magnetic field [34, 36, 40]. At low field, the MR is linear and parabolic dependent on the angle between the applied field and the sample surface, as typically observed in thin Fe_3O_4 granular films [7]. This different low-field behaviour is due to the different scattering probability for the tunnelling electrons when the grain magnetizations are parallel or perpendicular to the film plane [41]. In particular, the low field linear (quadratic) dependence of MR on the parallel (perpendicular) applied field can be explained by assuming an inter-granular (spin polarized)

electron tunnelling through antiferromagnetic boundaries [41]. The MR in granular magnetite is due to the tunnelling of spin polarized electrons between adjacent grains. When no magnetic field is applied, the magnetizations of the different grains are randomly oriented and the tunnelling between grains is not favoured, figure 9(b). When the magnetizations of the grains are aligned by applying an external magnetic field, then the spin polarized electrons have more states in which they can tunnel and the overall film resistance is reduced, figure 9(c). In the case of MR occurring in granular films, such as those discussed here, there is a very simple expression between the MR and the spin polarization P of the spin-polarized electrons governing the films conductivity. At saturation (M_S= 470 emu/cc), MR can be expressed as MR = $P^2/(1+P^2)$ [38]. For Fe28, considering the MR at RT (at maximum applied magnetic field), we estimate P= -16%, a value far below the predicted -100% spin polarization for bulk magnetite; the observation of a relatively low P for Fe_3O_4 thin films is not unusual [15].

Figure 10 evidences the relationship between the MR measured and the corresponding vacancy concentration (δ) as estimated with CEMS (table 3).

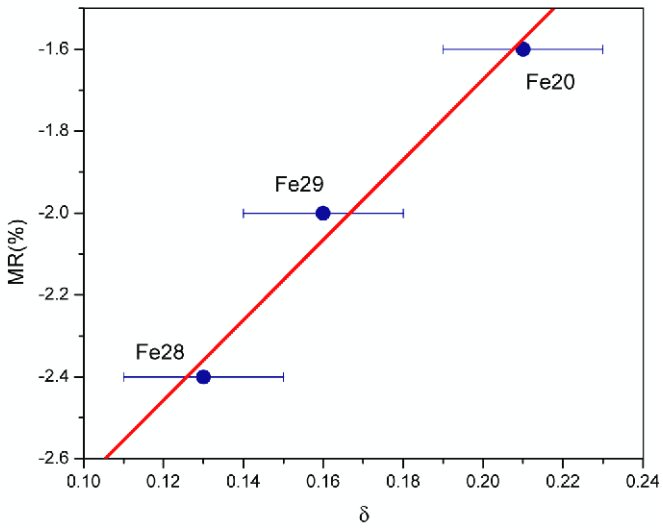

Figure 10. MR versus vacancy concentration (δ) obtained by CEMS for the studied samples. The MR is measured at RT and at 1.1 T magnetic field, applied parallel to the sample plane.

We observe an interesting correlation between the stoichiometry of the magnetite films and the corresponding MR properties. The highest (negative) MR value is obtained in the sample Fe28, which shows

the lowest δ value (table 3), while the most off-stoichiometric sample (Fe20) displays the lowest MR. Even if a more accurate study is needed in order to draw quantitative conclusions (more samples with different stoichiometry), we can certainly say that the fraction of the Fe^{3+} ions residing at the octahedral B site are critically influencing the magneto-electrical properties of (granular) $Fe_{3-\delta}O_4$ thin films. This is not surprising considering that the electrical conductivity in magnetite is fully determined by the electron hopping between the Fe^{2+} and Fe^{3+} ions residing at the B lattice site. Due to a relatively large error bar (figure 10), the comparison of the δ values for Fe28 and Fe29 is difficult, but the larger δ in Fe20 when compared to the other samples is a firm conclusion. Fe20 shows the largest grains among the different samples and the grains in Fe20 could be more subjected to surface oxidation when compared to those in Fe28 and Fe29. Since tunneling is an interface effect, the lower MR value in Fe20 when compared to other samples could be ascribed partly to the presence of a more deeply oxidized surface region.

The maximum MR theoretically predicted by Inoue *et al.* for inter-granular tunnelling of spin polarized carriers is 50 % [38]. Our data (figure 10) suggest that stoichiometry could partly influence the MR performances of the (granular) magnetite films. However, even for a perfectly stoichiometric Fe_3O_4, it seems not possible to achieve the maximum MR, if a linear correlation between δ and MR is assumed (figure 10). Indeed, other factors influence the MR response in (granular) magnetite films, such as a possible marked spin disorder at the grains surfaces that could make more difficult the surface spins alignment even if very large magnetic fields are applied [7, 15]. Spin disorder at grain interfaces has also been identified as the source of coercivity enhancements in ferrimagnetic spinel nanoparticles [42], and this observation is in accordance with the highest H_C and the lowest MR that we observe in sample Fe20 when compared to Fe28 and Fe29.

3.5. Inclusion of Fe_3O_4 in a trilayer stack for magnetic tunnel junction application.

Figure 11 shows the SQUID measurement for the $Fe_{3-\delta}O_4$/MgO/Co trilayer.

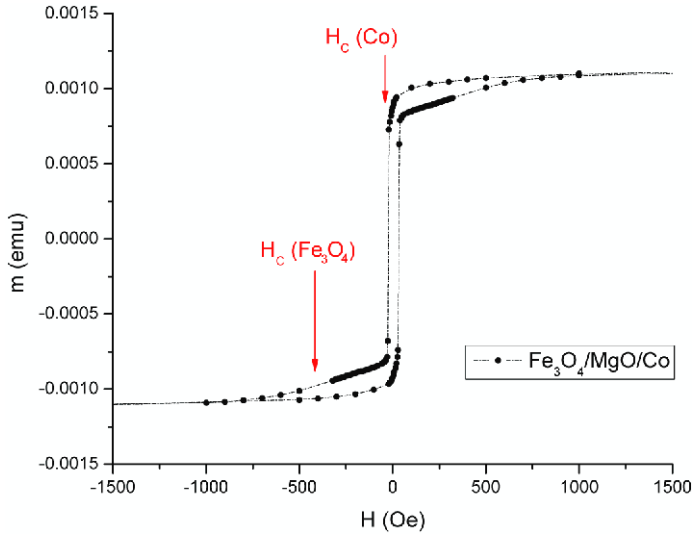

Figure 11. SQUID measurement of the Co(28.0 nm)/MgO(6.5 nm)/Fe_3O_4(16.1 nm) trilayer, showing two distinct switching field of the bottom ($Fe_{3-\delta}O_4$) and top (Co) layers.

The hysteresis curve of the selected $Fe_{3-\delta}O_4$/MgO/Co multilayer (figure 11) shows that the two magnetic layers are switching independently from one another in the applied field and have different coercivities. The magnetite switching field in figure 11 is lower than the H_C observed for a single layer of similar thickness (table 2 and figure 9), possibly due to coupling with the Co film. We also observe changes of the Co switching field when compared to single Co layers [17]; this is not surprising and it can be explained by the different substrate on top of which Co is deposited, giving a slightly different Co grain sizes. An optimization of material properties (i.e. films stoichiometry, interface roughness and grain sizes) as well as varying the magnetic film thickness will be pursed in order to obtain sharper and well distinct switching of ferromagnetic layers.

The results here reported are very encouraging in the prospect of a synthesis of MTJs based on the proposed stack. The AFM, XRR, ToF-SIMS results show that it is possible to produce Co/MgO/Fe_3O_4 trilayers on Si/SiO_2 substrates which are characterized by a low surface roughness of the magnetite layer, controlled interface roughness and good uniformity of the layers. SQUID measurements on the single layers (table 2) and the trilayer (figure 11) suggest that it is possible to control the $Fe_{3-\delta}O_4$ film thickness and the grain size in order to provide proper H_C for achieving an independent switching of the ferromagnetic layers magnetization in an external magnetic field. The interplay between the atomic-scale structural properties of magnetite and the carriers spin polarization could give a possible path for improving the performances of spintronic devices based on $Fe_{3-\delta}O_4$ thin films.

4. Conclusions

We have been successful in using the chemical synthesis route for depositing thin $Fe_{3-\delta}O_4$ polycrystalline films. Our structural and chemical characterizations show that the as-deposited magnetite films are of good quality with low level of contaminants (such as C). Magnetoresistance values up to -2.4 % at RT (at 1.1 T) has been observed. We have studied the influence of atomic-scale structural defects (vacancies) on the magnetotransport properties. Even though a more detailed study is needed in this direction, we have underlined a possible route for increasing the magnetoresistance properties of Fe_3O_4 thin films. The magnetotransport mechanism has been identified as due to the inter-granular tunnelling of spin-polarized carriers in the films. The switching field of the magnetite films, as measured by SQUID, is in well accordance with the field at which maximum resistance is observed in the magnetotransport characteristics. The grain size scales with film thickness influencing (together with vacancy concentration) the film coercivity, an aspect particularly important for the use of magnetite in spintronic devices. Our results show that the proposed simple and cost-effective deposition setup can be used for synthesizing $Fe_{3-\delta}O_4$ thin films displaying considerable spin polarized character (up to -16% at RT). A combined chemical vapour- and atomic layer- deposition process has been presented for the synthesis of Fe_3O_4/MgO/Co trilayers on Si/SiO_2 substrates. The hysteresis curve of selected trilayers shows two distinct switching fields, and this makes promising the synthesis of functional MTJ devices based on the proposed trilayered structure.

Acknowledgments

This work has been partly supported by the Cariplo Foundation in the framework of the SOLARIS (code n. 2004.1096) and SPAM^3 (code n. 2008.2363) projects. We acknowledge the work of Dr. Simone Cocco for the setting-up of the (CVD) deposition chamber and Dr. Roberto Fallica for his help in the MR measurements and for software development. We are indebted to Prof. Alessandro Lasciarfari at University of Pavia (Italy) for providing the access to the SQUID facility.

References

[1] Moskowitz B M, “Hitchhiker's Guide to Magnetism”, available online on the website of the “Institute for Rock Magnetism”, University of Minnesota, http://www.irm.umn.edu
[2] Yanase A and Siratori K 1984 J. Phys. Soc. Jpn. **53** 312.
[3] Zhang Z and S. Satpathy S 1991 Phys. Rev. B **44** 13319.
[4] Bibes M and A. Berthélémy A 2007 IEEE Trans. Electron. Devices **54** 1003.
[5] Fonin M, Dedkov Yu S, Pentcheva R, Rüdiger U, and Güntherodt G 2007 J. Phys.: Condens. Matter **19** 315217.
[6] Tobin J G, Morton S A, Yu S W, Waddill G D, Schuller I K, and Chambers S A 2007 J. Phys.: Condens. Matter **19** 315218.
[7] Liu H, Jiang E Y, and Bai H L 2003 Appl. Phys. Lett. **83** 3531.
[8] Tripathy D, Adeyeye A O, Boothroyd C B, Shannigrahi S 2008 J. Appl. Phys. **103** 07F701.
[9] Greullet F, Snoeck E, Tiusan C, Lacour D, Lenoble O, Magen C, and Calmels L 2008 Appl. Phys. Lett. **92** 53508.
[10] Kado T, Saito H, and K. Ando K 2007 J. Appl. Phys. **101** 09J511.
[11] T. Kado T 2008 Appl. Phys. Lett. **92** 092502.
[12] Y. Chen Y Z, Sun J R, Han Y N, Xie X Y, Shen J, Rong C B, He S L, and Shen B G, 2008 J. Appl. Phys. **103** 07D703.
[13] Singh M P, Carvello B, and Ranno L 2006 Appl. Phys. Lett. **89** 22504.
[14] Tripathy D and Adeyeye A O 2007 J. Appl. Phys. **101** 09J505.
[15] Lu Z L, Xu M X, Zou W Q, Wang S, Liu X C, Lin Y B, Xu J P, Lu Z H, Wang J F, Lv L Y, Zhang F M, and Du Y W 2007 Appl. Phys. Lett. **91** 102508.
[16] Sterbinsky G E, Cheng J, Chiu P T, Wessels B W, and Keavney D J 2007 J. Vac. Sci. Technol. B **25** 1389.
[17] Mantovan R, Georgieva M, Perego M, Lu H L, Cocco S, Zenkevich A, Scarel G, Fanciulli M 2007 Acta Physica Polonica A **112** 10.
[18] Boyd E P, Ketchum D R, Deng H, and Shore S G 1997 Chem. Mater. **9** 1154.
[19] Smith T W and Wychlck D 1960 J. Phys. Chem. **84** 1621.
[20] Niemeantsverdriet J W, Flipse C F J, Van der Kraan A M, and Van Loef J J 1982 Appl. Surf. Sci. **10** 302.
[21] Van Wonterghem J, Morup S, Charles S W, Wells S, and Villadsen J 1985 Phys. Rev. Lett. **55** 410.
[22] T.R.Thomas, Rough Surfaces, edited by Imperial College Press, London 1999.
[23]. Mantovan R and Fanciulli M 2007 Rev. Sci. Instrum. **78** 063902.
[24] PDF number 19-629, Inorganic Crystal Structure Database, National Institute of Standards and Technology (NIST) and Fachinformationszentrum Karlsruhe (FIZ), Edition 1-2008. Dvoryankina G G, Pinsker Z G 1962 J. Appl. Phys. **33** 1210.
[25] PDF number 33-664, Inorganic Crystal Structure Database, National Institute of Standards and Technology (NIST) and Fachinformationszentrum Karlsruhe (FIZ), Edition 1-2008. Sawada H 1996

Materials Research Bulletin **31** 141.

[26] PDF number 6-696, Inorganic Crystal Structure Database, National Institute of Standards and Technology (NIST) and Fachinformationszentrum Karlsruhe (FIZ), Edition 1-2008.

Kohlhaas R, Duenner P, Schmitz-Pranghe N 1967 Zeitschrift fuer Angewandte Physik **23** 245 and 1965 Transactions of the Metallurgical Society of Aime **233** 1519.

[27] Voogt F C, Hibma T, Zhang G L, Hoefman M, and Niesen L 1995 Surf. Sci. **331** 1508.

[28] De Grave E, Persoons R M, Vandenberghe R E, and de Bakker P M A 1993 Phys. Rev. B **47** 5881.

[29] Kale S, Bhagat S M, Lofland S E, Scabarozi T, Ogale S B, Orozco A, Shinde S R, Venkatesan T, Hannoyer B, Mercey B, and Prellier W 2001 Phys. Rev. B **64** 205413.

[30] Niu Z P, Wang Y, and Li F S 2006 Phys. Stat. sol (a) **203** 3705.

[31] Sawatzky G A, Van der Woude F, and Morrish A H 1969 Phys. Rev. **183** 383.

[32] Häggström L, Annersten H, Ericsson T, Wäppling R, Karner W, and Bjarman S 1978 Hyp. Int. **5** 201.

[33] Rogalski M, Besserguenev V, Barata N R A, and Baltazaer R 2003 IEEE Trans. Magn. **39** 00189464.

[34] Tripathy D, Adeyeye A O, Boothroyd C B, Piramanayagam S N 2007 J. Appl. Phys. **101** 013904.

[35] Hong J P, Lee S B, Jung Y W, Lee J H, Yoon K S, Kim K W, Kim C O, Lee C H, and Jung M H 2003 Appl. Phys. Lett. **83** 1590.

[36] Mi W B, Liu H, Li Z Q, Wu P, Jiang E Y, Bai H L 2006 J. Phys. D: Appl. Phys. **39** 5109.

[37] Park C, Peng Y, Zhu J G, Laughlin D E, and White R M 2005 J. Appl. Phys. **97** 10C303.

[38] Inoue J and Maekawa S 1996 Phys. Rev. B **53** R11927.

[39] Abeles B, Sheng P, Coutts M D, Arie Y 1975 Adv. Phys. **24** 407.

[40] Coey J M, Berkowitz A E, Balcells LI, Putris F F, and Parker F T 1998 Appl. Phys,. Lett. **72** 734.

[41] Eerenstein W, Palstra T T M, Hibma T, and Celotto S 2002 Phys. Rev. B **66** 201101(R).

[42] Kodama R H, Berkowitz A E 1999 Phys. Rev. B **59** 6321.